Room-Temperature Mid-Wave Infrared Guided-Mode Resonance Detectors

Abhilasha Kamboj, Leland Nordin, Aaron J. Muhowski, *Member, IEEE*, David Woolf, and Daniel Wasserman, *Senior Member, IEEE*

***Abstract*— We demonstrate room temperature mid-wave infrared detectors with high peak detectivity. Our detector structures consist of type-II superlattice nBn detectors with ultra-thin (∼ 250 nm) absorbers, integrated into an all-epitaxial guided-mode resonance architecture. The resulting devices show strong spectral selectivity, controlled by grating period, and low dark currents. We achieve room temperature TE-polarized peak specific detectivity (D^*) of $\approx 1.2 \times 10^{10}$ cm$\sqrt{\text{Hz}}$/W at $\lambda = 4.4\,\mu$m and $\approx 1 \times 10^{10}$ cm$\sqrt{\text{Hz}}/W$ at $\lambda = 4.7\,\mu$m, for grating periods of $\Lambda = 1.6\,\mu$m and $\Lambda = 1.8\,\mu$m, respectively. The presented all-epitaxial devices offer a unique approach to efficient room temperature mid-wave infrared detection with strong spectral and polarization selectivity.**

***Index Terms*— Photodetector, mid-infrared, superlattice, sensor.**

I. Introduction

THE mid-wave infrared (MWIR, $3-5\,\mu$m) is a technologically vital wavelength range with potential applications for gas sensing, free-space communication, and thermal imaging of hot objects. All of the above benefit from, or require, sensitive, high-operating-temperature (HOT) photodetectors. The current state of the art MWIR detectors are generally InSb or HgCdTe (MCT) photodiode detectors. InSb detectors often require cryogenic cooling in order to maintain acceptable dark currents, while MCT detectors suffer from growth non-uniformity and concerns regarding toxicity of their constituent materials. Recently, there has been significant interest in III-V type-II superlattice (T2SL) materials for mid-IR detection applications. T2SLs offer an effective band-gap controlled by choice of layer materials and thicknesses, have been predicted to benefit from reduced Auger recombination [1] and therefore lower dark currents, and can be integrated into a range of photodetector architectures, including p-i-n-junction photodiodes [2], bariode devices (such as nBn or CBIRD) [3], [4] or even phototransistors [5]. However, the spatial offset of electron and hole wavefunctions in T2SL materials results in a reduced absorption coefficient, when compared to bulk materials [6], [7]. Countering this reduced absorption requires thicker detectors, which, consequently, will increase detector dark current (noise) and reduce detector response times [8].

Accordingly, there has been interest in incorporating T2SL detectors into resonant optical structures in order to enhance the detector material's effective absorption coefficient [9]–[11]. Recently, it was demonstrated that MWIR T2SL nBn detectors could be integrated into guided-mode resonance (GMR) structures to allow for spectrally-selective detection with external quantum efficiency (EQE) of over 50% [12]. The GMR [13] structure is effectively a grating-capped dielectric waveguide, where at certain distinct frequencies (for a given polarization and incidence angle), the constructive/destructive interference between incident, transmitted, and scattered light results in sharp dips/peaks in transmission/reflection, making these structures of significant interest for light filtering applications across a wide range of wavelengths [14]–[16]. The initial ($T_{op} = 200$ K) demonstration of MWIR GMR T2SL detectors leveraged a low-index highly doped semiconductor layer beneath an nBn detector to form the waveguide structure, with the grating etched into a sacrificial GaSb layer grown above the nBn detector. These detectors, while showing excellent performance up to T = 200 K, degraded with increasing temperature and demonstrated anomalously large turn-on voltages (problematic for detector array operation). In the current work, we demonstrate room temperature (RT = 296 K) operation of redesigned MWIR GMR detectors, with enhanced EQE (EQE $\approx$ 60%), and peak TE-polarized specific detectivity, $D^* > 1 \times 10^{10}$ cm$\sqrt{\text{Hz}}$/W. In addition, our detectors show turn-on voltages less than −0.2V. The presented high EQE and high-detectivity devices offer a potentially transformative detector architecture for a range of vital mid-IR applications.

II. Device Design and Growth, Experimental Set-Up

The improved performance of the MWIR GMR photodetectors, compared to previous devices [12], results from changes to the device design and T2SL materials employed. First, the decrease in turn-on voltage was achieved by thinning our barrier layer, and p-doping the contact layer to create a tunnel-junction to the GaSb. The increase in T_{op} results from the

Manuscript received January 22, 2022; revised May 1, 2022; accepted May 5, 2022. Date of publication May 13, 2022; date of current version May 26, 2022. This work was supported in part by the United States Army under Contract W909MY-20-P-0010; in part by the National Science Foundation under Grant ECCS-1926187; and in part by the University of Texas Microelectronics Research Center (The Texas Nanofabrication Facility) through the National Nanotechnology Coordinated Infrastructure (NNCI) by the National Science Foundation under Grant ECCS-2025227. *(Corresponding author: Abhilasha Kamboj.)*

Abhilasha Kamboj, Leland Nordin, Aaron J. Muhowski, and Daniel Wasserman are with the Department of Electrical and Computer Engineering, The University of Texas at Austin, Austin, TX 78758 USA (e-mail: abhilashakamboj@utexas.edu; dw@utexas.edu).

David Woolf is with Physical Sciences Inc., Andover, MA 01810 USA.

Color versions of one or more figures in this letter are available at https://doi.org/10.1109/LPT.2022.3175110.

Digital Object Identifier 10.1109/LPT.2022.3175110

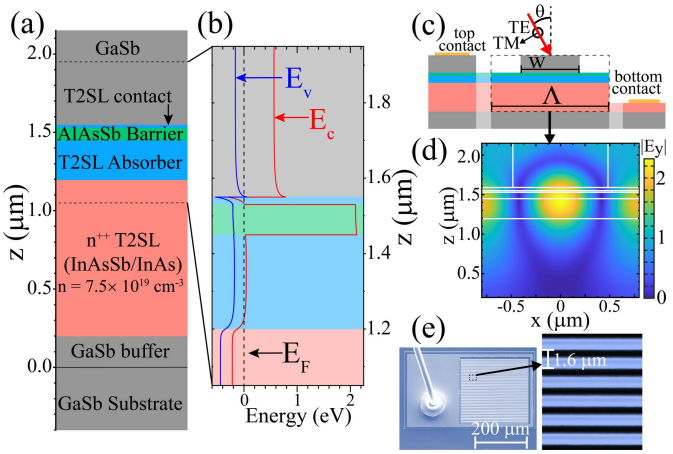

Fig. 1. (a) Growth stack for MWIR GMR detector structure and (b) band structure of nBn detector. (c) Cross-sectional schematic of a single period of the GMR detector, with location of top and bottom detector contacts shown on the left and right side, respectively. (d) Electric field profile of MWIR GMR structure for TE-polarized incident light of wavelength $\lambda = 4.44\,\mu$m. (e) Scanning electron micrograph of fabricated detector structure with expanded view of the $\Lambda = 1.6\,\mu$m gratings.

use of a shorter cut-off wavelength absorber ($\lambda_{co} \sim 5\,\mu$m), which dramatically reduces detector dark current J_{dark}. The T2SL period in this work is half of that in Ref. [12], to take advantage of the significantly higher absorption coefficients of short-period T2SLs [7]. Our devices were grown on a 2-inch lightly n-doped GaSb substrate in a Varian Gen II molecular beam epitaxy (MBE) system, beginning with a 200 nm n-doped GaSb buffer, followed by the device growth stack: a $1\,\mu$m thick highly doped n^{++} InAs/$InAs_{0.49}Sb_{0.51}$ T2SL, above which is grown the nBn detector structure, consisting of a 250 nm thick InAs/$InAs_{0.49}Sb_{0.51}$ T2SL (12 ML Period) absorber, an 80 nm thick unintentionally doped (UID) $AlAs_{0.08}Sb_{0.92}$ barrier and a 20 nm contact layer of the same T2SL material as the absorber. The structure is capped with a 600 nm thick UID GaSb layer. All superlattice layers have the same composition but different doping concentrations. The absorber is unintentionally doped (lightly n-doped), whereas the contact is p-doped to a concentration of 10^{18}cm^{-3}. The n^{++} T2SL layer serves as a low-index bottom cladding layer, where the high doping of the material reduces the permittivity according to the Drude formalism, which provides an accurate mechanism for calculating the dielectric response of highly-doped semiconductors in the mid-IR [17]. Although it uses the same T2SL as the detector absorber, state-filling and ultra-fast non-radiative recombination times [18] in the n^{++} layer ensures that it does not contribute to the optical response of the detector. The top GaSb layer serves as the high-index grating material. The device layer stack and band structure are shown in Fig. 1(a-b).

Fig. 1(c) & (e) show the cross-sectional schematic and scanning electron micrograph (SEM) of a fabricated device, respectively. Top (bottom) contacts (Ti/Pt/Au, 40/15/180 nm) are patterned and deposited above (around) an etched mesa. Gratings of period $\Lambda = 1.6$ and $1.8\,\mu$m are etched into the top GaSb layer of the mesa, to within 10's of nm of the nBn contact layer. Grating devices are compared to a control sample for which the entire top GaSb layer of the mesa is etched to the same depth as the gratings. The fabricated devices are mounted and wire-bonded to leadless chip carriers (LCC). Temperature-dependent dark current-voltage measurements are made with a copper shield (to block any external light from the device) attached to the cold-finger upon which the LCC is mounted. The GMR detector spectral response is measured using a Bruker Vertex 80v Fourier-transform infrared (FTIR) spectrometer, and normalized to the calibrated, known response of commercial detectors, to account for the spectral weighting of the FTIR output beam. The detector signal resulting from the emission from a calibrated 1000 °C blackbody source, modulated by an optical chopper, and passing through a variable aperture and a $3.6\,\mu$m bandpass filter, is then measured. We then calculate the wavelength dependent EQE by scaling the normalized FTIR spectra by the responsivity measured at $\lambda = 3.6\,\mu$m.

Detector response is modeled using rigorous coupled-wave analysis (RCWA) [19], which solves for reflection and transmission, as well as the optical fields in our structures, as a function of wavelength, incidence angle and polarization. The n^{++} T2SL is modeled as a Drude metal with plasma wavelength $\lambda_p = 5.7\,\mu$m and scattering rate $\gamma = 1 \times 10^{13}$ rad s^{-1}. The real parts of the permittivity for the T2SL layers and barrier are determined from a weighted average of their constituent materials. The complex permittivity of our T2SL absorber is estimated by fitting RCWA simulations to the experimental spectral response of our control device (nBn device with only 20 nm planar GaSb layer on top), using the detector absorption coefficient $\alpha(\lambda)$ as our fitting parameter, assuming an anisotropic absorption coefficient where only the in-plane components of α are non-zero [20]. The extracted α at $\lambda = 4.4\,\mu$m is 3100cm^{-1}, in line with the expected absorption coefficient of short period T2SLs [21]. We use the simulated field profiles to model the detector EQE by calculating the difference between the Poynting flux at the barrier/absorber and absorber/n^{++} interfaces. Because the typical diffusion length associated with T2SL materials is significantly longer than our absorber thickness [22], we assume a 100% collection efficiency of photo-generated charge carriers. The model considers light directly transmitted through the detector and reflected from the backside of the wafer. The lightly n-doped GaSb substrate absorption coefficient is modeled with a combination of electron free carrier absorption and inter-valley conduction band absorption [23] verified with reflectance and transmittance measurements on a bare GaSb wafer. Our simulations suggest that $\sim 2\%$ of our peak EQE results from backside reflection.

III. Results and Discussion

Fig. 2(a) shows the dark current as a function of temperature from a representative $\Lambda = 1.8\,\mu$m grating detector. A clear turn-on is seen in the devices at a reverse bias as low as -0.1V as shown in the inset of Fig. 2(b) where the T = 296 K device responsivity, at the bandpass wavelength $\lambda_{BP} = 3.6\,\mu$m, is plotted as a function of the applied bias. The dark current remains largely constant for reverse biases larger than

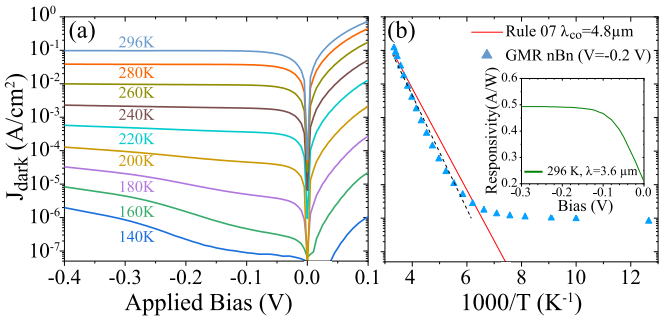

Fig. 2. (a) MWIR GMR nBn detector dark current density, J_{dark} for temperatures from 140 K to 296 K. (b) Arrhenius plot of dark current (blue triangles) at $V = -0.2\ V$. From this plot, we can extract the effective cut-off wavelength of our detector at room temperature (dashed line, $\lambda_{co} = 4.8\,\mu$m). Also plotted is the predicted dark current for an MCT detector with $\lambda_{co} = 4.8\,\mu$m using the Rule 07 heuristic (red solid line). Inset shows device T=296 K responsivity vs. applied bias at $\lambda_{BP} = 3.6\,\mu$m.

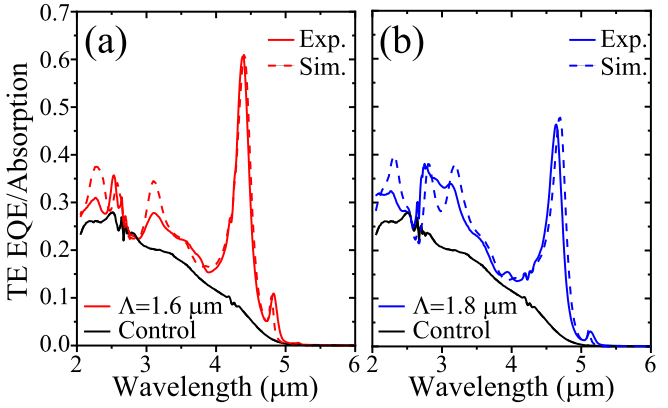

Fig. 3. TE-polarized experimental (solid) and modeled (dashed) external quantum efficiency for the (a) $\Lambda = 1.6\,\mu$m (red) and (b) $\Lambda = 1.8\,\mu$m (blue) grating detector devices. The EQE from an unpatterned control sample (black) is shown in (a) and (b) for comparison. Because the absorption coefficient is determined by fitting the control response, the modeled and experimental control EQE overlap. The TM-polarized response of the grating devices (not shown) is similar to that of the control devices.

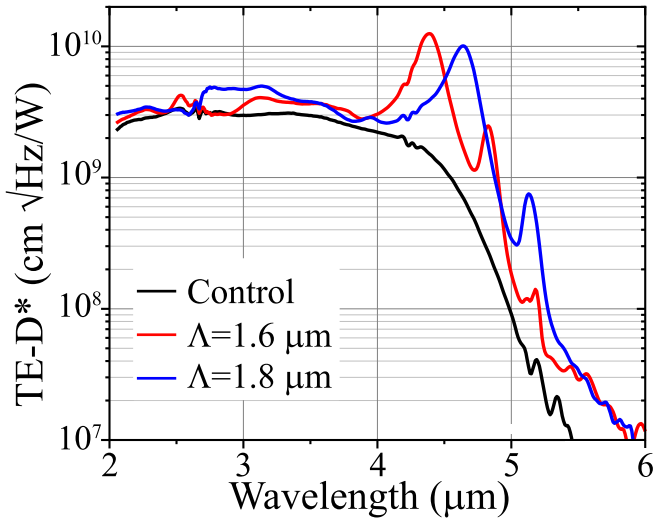

Fig. 4. Room temperature TE-polarized estimated specific detectivity (D^*) of the control (black), and the $\Lambda = 1.6\,\mu$m (red) and $\Lambda = 1.8\,\mu$m (blue) grating detector devices.

-0.2V, indicative of diffusion current dominating the total dark current. As the dark current densities of a photodetector are proportional to the thickness of the absorber (in diffusion-limited operation), the ultra-thin GMR detectors are expected to have significantly lower dark current than much thicker photodetectors operating at the same wavelength. This is evident in Fig. 2(b), where the dark current (at $V = -0.2$V) vs. temperature is compared to the predicted current for an ideal MCT detector calculated using the so-called "Rule 07" [24], a heuristic often used as a benchmark for mid-IR detector dark currents. While our detector dark currents do not approach the recently demonstrated dark currents from MCT detectors leveraging carrier depletion Auger suppression [25], they are below or comparable to Rule 07 for temperatures above 160 K, and well below those of typical III-V semiconductor MWIR photodetectors [26], [27].

The experimental EQE at $T_{op} = 296$ K for the $\Lambda = 1.6\,\mu$m and $\Lambda = 1.8\,\mu$m grating period detectors, as well as the control sample, are shown in Fig. 3, for TE-polarized incident light. Strong peaks in EQE are seen in both grating period samples. For the $\Lambda = 1.6\,\mu$m sample, peak EQE is observed at $\lambda = 4.4\,\mu$m, reaching a peak value of $\sim 60\%$, a factor of $\times$ 7.5 enhancement over the unpatterned control sample. For the $\Lambda = 1.8\,\mu$m sample, peak EQE is observed at $\lambda = 4.7\,\mu$m, reaching a maximum value of $\sim 46\%$, a factor of $\times$ 14 enhancement over the unpatterned control sample. Tuning the detector grating period allows for peak response across the MWIR. Moreover, we observe a substantial enhancement of detector response, with particularly strong enhancement at or near the bandedge of the T2SL absorber. Typically, absorption at the bandedge of a T2SL is weak, and if efficient detection is required at a specific wavelength, λ_0, it is often necessary to use an absorber cut-off wavelength (λ_{co}) much longer than λ_0. Such an approach comes with trade-offs however, as dark current is exponential in absorber cut-off wavelength, so that specific detectivity (D^*) gains due to increased EQE are offset by increased J_{dark}. The GMR MWIR detector architecture thus allows for a strong enhancement of EQE at or near the absorber bandedge, without having to resort to longer λ_{co}, effectively decoupling the dark current/EQE trade-off intrinsic in the majority of MWIR detector materials and architectures.

In Fig. 4, we present the estimated (TE-polarized) specific detectivity of our room temperature MWIR GMR detectors. Specific detectivity is calculated with the expression, $D^* = R_i\sqrt{\frac{A}{2q|I|+4\ k_bT/R}}$, from the experimentally measured detector current, dynamic resistance, and responsivity (I, $R = dV/dI$, and R_i, respectively), mesa area A, electronic charge q, Boltzmann's constant k_b, and temperature T. We obtain peak specific detectivity of 1.2×10^{10} and 1×10^{10} cm$\sqrt{\text{Hz}}$/W for the $\Lambda = 1.6$ and $1.8\,\mu$m period detectors respectively, with substantial enhancement in D^* observed at wavelengths near the absorber's bandedge, $\lambda \approx 5\,\mu$m. The TM-polarized response (not shown) is similar to that of the control, with minimal enhancement at features associated with GMR resonances,

a result of the anisotropic absorption coefficient of the T2SL. While we use 1D grating structures here, to more clearly identify GMR features of the optical response, future detectors could easily leverage 2D arrays of GaSb pillars for polarization independent response, and/or the addition of micro- or immersion-lenses to increase light collection [28].

IV. Conclusion

In conclusion, we have demonstrated enhanced MWIR detectors operating at room temperature (296 K). Leveraging an ultra-thin nBn detector architecture engineered for MWIR absorption at room temperature, we can substantially reduce detector dark current allowing for high-temperature operation. At the same time, by integrating our detectors into guided-mode resonance structures, we can enhance the detector response substantially, especially near detector cut-off. We demonstrate TE-polarized peak EQE $\approx$ 60% (46%) for $\Lambda = 1.6\,\mu$m ($1.8\,\mu$m) grating GMR devices with $> \times 7.5$ ($\times 14$) enhancement, when compared to the unpatterned control sample, at $\lambda = 4.4\,\mu$m ($4.7\,\mu$m), near detector cut-off. We also show estimated peak specific detectivity, $D^* \approx 1.2 \times 10^{10}$ and 1×10^{10} cm$\sqrt{\text{Hz}}$/W for the 1.6 and 1.8 μm period grating-patterned detectors, respectively, exceeding that of state-of-the-art III-V RT MWIR detectors. The all-epitaxial approach presented here allows us to embed opto-electronic functionality in resonant optical structures, with strongly enhanced performance across the technologically vital MWIR. The ability to efficiently detect MWIR light with room temperature sensors could have significant implications for gas sensing, thermal imaging, or even free-space communication applications.

Acknowledgment

Any opinions, findings, and conclusions or recommendations expressed in this material are those of the author(s) and do not necessarily reflect the views of the U.S. Army.

References

[1] C. H. Grein, M. E. Flatté, J. T. Olesberg, S. A. Anson, L. Zhang, and T. F. Boggess, "Auger recombination in narrow-gap semiconductor superlattices incorporating antimony," *J. Appl. Phys.*, vol. 92, no. 12, pp. 7311–7316, 2002.

[2] H. Mohseni, M. Razeghi, G. J. Brown, and Y. S. Park, "High-performance InAs/GaSb superlattice photodiodes for the very long wavelength infrared range," *Appl. Phys. Lett.*, vol. 78, no. 15, pp. 2107–2109, Apr. 2001.

[3] J. B. Rodriguez *et al.*, "nBn structure based on InAs/GaSb type-II strained layer superlattices," *Appl. Phys. Lett.*, vol. 91, no. 4, 2007, Art. no. 043514.

[4] D. Z.-Y. Ting *et al.*, "A high-performance long wavelength superlattice complementary barrier infrared detector," *Appl. Phys. Lett.*, vol. 95, no. 2, 2009, Art. no. 023508.

[5] A. Haddadi, S. Adhikary, A. Dehzangi, and M. Razeghi, "Mid-wavelength infrared heterojunction phototransistors based on type-II InAs/AlSb/GaSb superlattices," *Appl. Phys. Lett.*, vol. 109, no. 2, Jul. 2016, Art. no. 021107.

[6] A. Rogalski, P. Martyniuk, and M. Kopytko, "Type-II superlattice photodetectors versus HgCdTe photodiodes," *Prog. Quantum Electron.*, vol. 68, Nov. 2019, Art. no. 100228.

[7] I. Vurgaftman *et al.*, "Interband absorption strength in long-wave infrared type-II superlattices with small and large superlattice periods compared to bulk materials," *Appl. Phys. Lett.*, vol. 108, no. 22, May 2016, Art. no. 222101.

[8] B. V. Olson *et al.*, "Minority carrier lifetime and dark current measurements in mid-wavelength infrared $InAs_{0.91}Sb_{0.09}$ alloy nBn photodetectors," *Appl. Phys. Lett.*, vol. 107, no. 18, Nov. 2015, Art. no. 183504.

[9] J. A. Nolde *et al.*, "Resonant quantum efficiency enhancement of midwave infrared nBn photodetectors using one-dimensional plasmonic gratings," *Appl. Phys. Lett.*, vol. 106, no. 26, Jun. 2015, Art. no. 261109.

[10] M. D. Goldflam *et al.*, "Enhanced infrared detectors using resonant structures combined with thin type-II superlattice absorbers," *Appl. Phys. Lett.*, vol. 109, no. 25, Dec. 2016, Art. no. 251103.

[11] V. Letka, A. Bainbridge, A. P. Craig, F. Al-Saymari, and A. R. J. Marshall, "Resonant cavity-enhanced photodetector incorporating a type-II superlattice to extend MWIR sensitivity," *Opt. Exp.*, vol. 27, no. 17, pp. 23970–23980, 2019.

[12] A. Kamboj, L. Nordin, P. Petluru, A. J. Muhowski, D. N. Woolf, and D. Wasserman, "All-epitaxial guided-mode resonance mid-wave infrared detectors," *Appl. Phys. Lett.*, vol. 118, no. 20, May 2021, Art. no. 201102.

[13] S. S. Wang and R. Magnusson, "Theory and applications of guided-mode resonance filters," *Appl. Opt.*, vol. 32, no. 14, pp. 2606–2613, May 1993.

[14] A. Szeghalmi, M. Helgert, R. Brunner, F. Heyroth, U. Gösele, and M. Knez, "Tunable guided-mode resonance grating filter," *Adv. Funct. Mater.*, vol. 20, no. 13, pp. 2053–2062, Jul. 2010.

[15] Y. Zhong *et al.*, "Mid-wave infrared narrow bandwidth guided mode resonance notch filter," *Opt. Lett.*, vol. 42, no. 2, pp. 223–226, 2017.

[16] T. Kondo, S. Ura, and R. Magnusson, "Design of guided-mode resonance mirrors for short laser cavities," *J. Opt. Soc. Amer. A, Opt. Image Sci.*, vol. 32, no. 8, pp. 1454–1458, 2015.

[17] S. Law, D. C. Adams, A. M. Taylor, and D. Wasserman, "Mid-infrared designer metals," *Opt. Exp.*, vol. 20, no. 11, pp. 12155–12165, 2012.

[18] E. A. Kadlec *et al.*, "Effects of electron doping level on minority carrier lifetimes in n-type mid-wave infrared InAs/$InAs_{1-x}Sb_x$ type-II superlattices," *Appl. Phys. Lett.*, vol. 109, no. 26, Dec. 2016, Art. no. 261105.

[19] V. A. Podolskiy. *A Versatile Implmentation of the Rigorous Coupled Wave Analysis*. Accessed: May 26, 2017. [Online]. Available: http://faculty.uml.edu/vpodolskiy/codes/index.html

[20] T. Manyk, K. Michalczewski, K. Murawski, P. Martyniuk, and J. Rutkowski, "InAs/InAsSb strain-balanced superlattices for longwave infrared detectors," *Sensors*, vol. 19, no. 8, p. 1907, Apr. 2019.

[21] P. T. Webster *et al.*, "Absorption properties of type-II InAs/InAsSb superlattices measured by spectroscopic ellipsometry," *Appl. Phys. Lett.*, vol. 106, no. 6, Feb. 2015, Art. no. 061907.

[22] D. Zuo *et al.*, "Direct minority carrier transport characterization of InAs/InAsSb superlattice nBn photodetectors," *Appl. Phys. Lett.*, vol. 106, no. 7, Feb. 2015, Art. no. 071107.

[23] A. Chandola, R. Pino, and P. S. Dutta, "Below bandgap optical absorption in tellurium-doped GaSb," *Semicond. Sci. Technol.*, vol. 20, no. 8, pp. 886–893, Aug. 2005.

[24] W. E. Tennant, D. Lee, M. Zandian, E. Piquette, and M. Carmody, "MBE HgCdTe technology: A very general solution to IR detection, described by 'rule 07', a very convenient heuristic," *J. Electron. Mater.*, vol. 37, no. 9, pp. 1406–1410, 2008.

[25] D. Lee *et al.*, "Law 19: The ultimate photodiode performance metric," *Proc. SPIE*, vol. 11407, pp. 93–105, May 2020.

[26] A. P. Craig, V. Letka, M. Carmichael, T. Golding, and A. R. Marshall, "InAsSb-based detectors on GaSb for near-room-temperature operation in the mid-wave infrared," *Appl. Phys. Lett.*, vol. 118, no. 25, Jun. 2021, Art. no. 251103.

[27] J. Kim *et al.*, "HOT MWIR InAs/InAsSb T2SL discrete photodetector development," *Proc. SPIE*, vol. 10624, pp. 108–115, May 2018.

[28] A. Soibel *et al.*, "High operating temperature nBn detector with monolithically integrated microlens," *Appl. Phys. Lett.*, vol. 112, no. 4, Jan. 2018, Art. no. 041105.